ELSEVIER

Journal of Fluids and Structures 22 (2006) 327–344

JOURNAL OF FLUIDS AND STRUCTURES

www.elsevier.com/locate/jfs

Numerical experiments on vortex shedding from an oscillating cylinder

F.L. Ponta[a,*], H. Aref[b]

[a]Department of Theoretical and Applied Mechanics, University of Illinois at Urbana-Champaign, Urbana, IL 61801, USA
[b]Department of Engineering Science and Mechanics, Virginia Polytechnic Institute & State University, Blacksburg, VA 24061, USA

Received 9 June 2004; accepted 26 November 2005

Abstract

Vortex street wakes behind a cylinder oscillating in a steady free stream have been studied experimentally and numerically by several authors. Williamson and Roshko attempted a classification of the various wake patterns observed as a function of two dimensionless parameters, the wavelength of the undulatory motion of the cylinder scaled by the cylinder diameter and the amplitude of the transverse undulations scaled by cylinder diameter. Several qualitatively distinct wake regimes were observed experimentally. These were classified in terms of the vortex patterns, e.g., two singlets, two pairs, pair and singlet, and so on. The main series of experiments was conducted at $\mathrm{Re} = 392$. Here, we construct a numerical method that allows us to perform corresponding numerical experiments at lower values of Reynolds number. We document the accuracy of the numerical method by comparing to well-established results for vortex wakes behind fixed cylinders. We then perform a number of numerical experiments for $\mathrm{Re} = 140$ and establish several points of correspondence with the experiments. Our simulation results also shed light on the classification scheme of Williamson and Roshko and suggest how this classification may change with Reynolds number. We find remarkable sensitivity to details of the oscillation of the cylinder, in particular whether the oscillation takes place at fixed streamwise velocity or at fixed cylinder speed along its trajectory.

Keywords: Vortex street; Oscillating cylinder; Vorticity–velocity formulation; Finite element method

1. Introduction

In addition to the familiar Kármán vortex street behind a stationary cylinder in a uniform stream, several more complex vortex patterns have been observed in the wakes of oscillating cylinders. There is a large body of literature on experimental studies of vortex wakes behind cylinders oscillating either normally or in-line with the uniform stream [see Khalak and Williamson (1999) for further references]. An attempt at classifying such vortex patterns has been made by Williamson and Roshko (1988), henceforth referred to as WR, using a symbolic code of letters and numbers that describes the combination of pairs and single vortices shed during each cycle of the forced oscillation of the cylinder. For example, 2S indicates two single vortices shed per cycle, 2P indicates two vortex pairs shed per cycle, P + S signifies a pattern in which one pair and a single vortex are shed in each cycle, and so on. WR gave a map of when the various

*Corresponding author. Present address: College of Engineering, University of Buenos Aires, USA.
E-mail addresses: ponta@uiuc.edu, fponta@fi.uba.ar (F.L. Ponta).

0889-9746/$ - see front matter © 2006 Elsevier Ltd. All rights reserved.
doi:10.1016/j.jfluidstructs.2006.02.001

vortex patterns would occur using a nondimensional wavelength–amplitude plane. We have used their classification and map as a basis for our computational study.

Two major issues arise from the WR study. The first, recalled in Khalak and Williamson (1999), is the difference between shedding patterns at low and at high Reynolds numbers which, to a large extent, remains unanswered. The second is the role of three-dimensional disturbances. WR concentrated on higher values of Reynolds number, exploring the value $Re = 392$ in particular detail. For $300 < Re < 1000$ (which corresponds to a mildly turbulent wake) the vortex synchronization regions in the wavelength–amplitude map of WR apparently remain invariant. On the other hand, for $Re < 200$ (which corresponds to the laminar regime accessible to our numerical experiments) the boundaries between the various regions appear to shift, and the 2P mode disappears altogether, with the P + S mode taking its place. Khalak and Williamson (1999) remarks that for experiments on vortex-induced oscillation as well the flow at low Re behaves differently from high Re flow. In this case, one of the modes of the amplitude response (the so-called *upper branch*) disappears. The authors suggest that the two phenomena (i.e., P + S replacing 2P for forced oscillation of the cylinder and the suppression of the upper branch mode for vortex-induced oscillation) may be related. Those observations are consistent with other experimental studies both for forced and free oscillations [Griffin and Ramberg (1974), Anagnostopoulos and Bearman (1992), among others], where in the low-Reynolds-number regime the 2P mode is never observed for forced oscillations and the upper-branch is never observed in vortex-shedding-induced oscillations. The role of three-dimensional disturbances is more difficult to assess. In an experiment three-dimensional disturbances are, of course, a fact of life. In a simulation based on the two-dimensional Navier–Stokes equations, three-dimensional disturbances are impossible. When comparing the results of a low Reynolds number, two-dimensional simulation to a higher-Reynolds number laboratory experiment, there are several sources that may be responsible for observed differences.

Besides the experimental work referenced above, we mention some analytical and computational work on complex wake structures of forced and freely oscillating cylinders. Aref and Stremler (1996) applied their analysis of the motion of three-point vortices with zero net circulation in a periodic strip to the observations of WR of the P + S wake and were able to find reasonable correspondence with the experimental results although several parameters (e.g., the vortex circulations) could be adjusted. This analysis suggested that many additional possibilities, so far not observed experimentally, exist for the vortex structure of the wake behind an oscillating cylinder. We have begun referring to such vortex patterns as "*exotic wakes*". Several direct numerical simulation studies have been performed on freely oscillating cylinders for Re up to 350 [see Khalak and Williamson (1999) for a list of references]. We mention Mittal and Tezduyar (1992) and Mittal and Kumar (1999), who studied the vortex-induced in-line and cross-flow oscillations of a cylinder using a deforming spatial domain/stabilized space–time finite element formulation of the Navier–Stokes equation. Newman and Karniadakis (1996, 1997) and Evangelinos and Karniadakis (1999) studied the wake of flexible and rigid cylinders and cables subject to vortex-induced vibrations using spectral elements to discretize the cross-sectional plane with a Fourier expansion in the spanwise direction. These works are consistent with the low Re experiments for free vibration that do not exhibit an upper branch mode of the amplitude response. They only find the 2S mode throughout the lock-in regime. On the other hand, the P + S mode has been found in low Re simulations of forced oscillations: Meneghini and Bearman (1995) used the discrete vortex-in-cell formulation, a two-dimensional hybrid numerical method where convection of vorticity is modelled in a Lagrangian way incorporating viscous diffusion by an Eulerian scheme. They solved the problem in a frame of reference fixed to the cylinder, imposing an oscillating cross-flow. Blackburn and Henderson (1996) presented two-dimensional numerical simulations of vortex-induced and forced cross-flow oscillations using a spectral element spatial discretization with a stiffly stable time integration scheme to solve the Navier–Stokes equation in an accelerating frame of reference attached to the cylinder.

In this paper, we primarily study the periodic vortex structures produced in the wake of a cylinder subject to forced oscillations at low Re, exploring in particular the phenomenon of the P + S structure. To this end, we have developed a new numerical approach that we introduce in Section 2. To validate our approach and numerical code, we explored the Strouhal number versus Reynolds number curve for our computed vortex street wakes for a stationary cylinder in the range $50 < Re < 180$, finding excellent agreement with this well-established empirical relationship. Armed with these benchmarking results, we experiment with wakes of oscillating cylinders in Section 3, and we explore a section of the WR map at $Re = 140$, identifying similarities and differences with the higher Re results reported in WR. Our concluding Section 4 contains discussion and outlook for further work.

2. The kinematic Laplacian equation method

In this section, we shall introduce a new type of vorticity–velocity method based on a space–time splitting of the problem that solves the time evolution of the vorticity as an ordinary differential equation on each node of the spatial

discretization. The input for the vorticity transport equation at each time-step is computed from the spatial solution for the velocity field provided by a linear PDE expression in weak form called the *kinematic Laplacian equation* (henceforth referred to as KLE). The input of the KLE being provided by the time integration of the vorticity.

A comprehensive description of the mathematics and numerical implementation of the KLE method can be found in Ponta (2005). Here, we summarize the most essential points in order for this paper to be self-contained.

2.1. Hybrid vorticity–velocity formulation

During the last three decades several studies appeared concerning the representation of the Navier–Stokes equations in terms of nonprimitive variables (namely the vorticity and the velocity potentials) instead of the classical formulation in terms of the primitive variables (velocity and pressure). This family of approaches is generally known as vorticity-stream function $(\boldsymbol{\omega}, \boldsymbol{\psi})$ methods. More recently, together with those works on the vorticity-stream function formulation and as a natural extension of them, a comparatively smaller number of studies were presented using a hybrid formulation in terms of the primitive and nonprimitive variables velocity and vorticity. As several authors pointed out (Quartapelle, 1993; Clercx, 1997; Speziale, 1987), the vorticity–velocity $(\boldsymbol{\omega}, \boldsymbol{v})$ methods (as they are generally known) present some advantages compared with the classical formulation on primitive variables or with the vorticity-stream function methods, namely: (a) The pair of variables involved is particularly suited for a dynamic description of incompressible viscous flows. The vorticity is governed by a well understood dynamical equation while the velocity, which embodies the kinematical aspect of the problem, can be related to the vorticity by a simple elliptic equation. In vortex-dominated flows the vorticity advection is a fundamental process determining the dynamics of the flow, hence the vorticity–velocity description is closer to physical reality. (b) The variety of boundary conditions that can be chosen for the velocity potentials due to the nonuniqueness of the velocity representation is avoided since the velocity is supplemented by unique boundary conditions. (c) In some specific situations like that of external flows, boundary conditions at infinity are easier to implement for the vorticity than for the pressure. (d) The noninertial effects only enter the solution procedure of the $(\boldsymbol{\omega}, \boldsymbol{v})$ formulation via the proper implementation of the initial and boundary conditions. Hence, the general applicability of an algorithm based on the $(\boldsymbol{\omega}, \boldsymbol{v})$ formulation is enhanced because it is independent of whether or not the frame of reference is inertial.

The first uses of the $(\boldsymbol{\omega}, \boldsymbol{v})$ formulation of the incompressible Navier–Stokes equations were reported by Fasel (1976) who analyzed the stability of boundary layers in two dimensions and by Dennis et al. (1979) who derived a numerical method for computing steady-state three-dimensional flows. Both approaches were based on finite difference techniques. Since then several investigations have been conducted on incompressible hybrid variable models using variations of the finite difference approach [e.g. see Gatski et al. (1989), Napolitano and Pascazio (1991), Guj and Stella (1993)]. A vorticity–velocity finite element solution of the three-dimensional compressible Navier–Stokes equations have been presented by Guevremont et al. (1993) who investigated the steady state flow in a cubic cavity for several Mach numbers. More recently Clercx (1997), then Davies and Carpenter (2001), introduced pseudospectral procedures for the $(\boldsymbol{\omega}, \boldsymbol{v})$ formulation. Lo and Young (2004) presented an arbitrary Lagrangian–Eulerian $(\boldsymbol{\omega}, \boldsymbol{v})$ method for two-dimensional free surface flow, using finite difference discretization for the free surface and finite element discretization for the interior of the domain.

A disadvantage of the vorticity–velocity formulation, compared with the formulation in primitive variables is that in the most general three-dimensional case the $(\boldsymbol{\omega}, \boldsymbol{v})$ formulation requires a total of six equations to be solved instead of the usual four of the primitive-variable approach (Clercx, 1997). The KLE method is characterized by a complete decoupling of the two variables in a vorticity-in-time/velocity-in-space split algorithm, thus reducing to three the number of unknowns to solve in the time integration process. This time–space splitting also favors the use of adaptive variable-stepsize/variable-order ODE algorithms which enhances the efficiency and robustness of the time integration process.

A comprehensive study of the theoretical basis of the vorticity–velocity formulation in two and three dimensions can be found in Quartapelle (1993, Chapter 4), including a series of theorems proving the equivalence between the $(\boldsymbol{\omega}, \boldsymbol{v})$ formulation of the incompressible Navier–Stokes equations and their classical formulation in primitive variables (velocity–pressure).

2.2. Vorticity boundary conditions

A common problem to all the methods based on nonprimitive or hybrid variables is the absence of boundary conditions for the vorticity in presence of no-slip boundary conditions for the velocity. In the case of the $(\boldsymbol{\omega}, \boldsymbol{\psi})$ formulation it also implies that the Poisson problem for the stream function with both Dirichlet and Neumann

conditions is overdetermined. There are several different ways of overcoming this difficulty. Some earlier approaches like the *boundary vorticity formula* or the *vorticity creation* methods use different techniques to define the boundary values of vorticity in terms of the stream function (or the velocity) by means of some approximate formula applied locally at the no-slip boundary. They are roughly equivalent, however their implementation may differ remarkably depending on the type of discretization used (Quartapelle, 1993; Anderson, 1988; Chorin, 1973, 1978).

An alternative viewpoint have been introduced by Quartapelle and Valz-Gris (1981) and Quartapelle (1981). They showed that in order to satisfy the no-slip boundary conditions for the velocity, the vorticity should be subject to an integral constraint. This integral condition enforces the orthogonality of the abstract projection of the vorticity field with respect to the linear space of the harmonic functions defined on the domain. This condition is a direct consequence of the boundary conditions on the velocity, and ensure satisfaction of essential conservation laws for the vorticity. An important aspect of the integral vorticity conditions is their nonlocal character: the vorticity distribution in the interior of the domain and on its boundary is affected at each time by the instantaneous values of the tangential and normal components of the velocity along the entire boundary. In other words, the distribution of the vorticity in the whole domain is constrained by the velocity boundary values. A detailed description of the mathematical basis and the different numerical implementations of the orthogonal-projection operation of the vorticity field for the $(\boldsymbol{\omega}, \boldsymbol{\psi})$ formulation can be found in Quartapelle (1993).

In our method, the issue of the vorticity boundary conditions on the no-slip surface is dealt with by a sequence of two solutions of the KLE under a different set of velocity boundary conditions. Thus, inside each time step, we perform two projectional operations of integral character applied on the velocity field which ensures that the vorticity evolves in time in a way compatible with the time-dependent velocity boundary values.

2.3. The Laplacian approach as a $(\boldsymbol{\omega}, \boldsymbol{v})$ method: the KLE

Starting from the well-known vector identity

$$\nabla^2 \boldsymbol{v} = \boldsymbol{\nabla}\cdot\boldsymbol{\nabla}\boldsymbol{v} = \boldsymbol{\nabla}(\boldsymbol{\nabla}\cdot\boldsymbol{v}) - \boldsymbol{\nabla}\times(\boldsymbol{\nabla}\times\boldsymbol{v}), \tag{1}$$

we found that a variational form of this "Laplacian" expression could be advantageously used as the spatial counterpart of the vorticity transport equation in a new type of vorticity–velocity method.

Let us consider the full three-dimensional incompressible Navier–Stokes equation in vorticity form for a flow domain Ω with solid boundary $\partial\Omega$ and *external* boundary of Ω in the far field, in a moving frame of reference fixed to the solid,

$$\frac{\partial \boldsymbol{\omega}}{\partial t} = -\boldsymbol{v}\cdot\boldsymbol{\nabla}\boldsymbol{\omega} + \nu\nabla^2\boldsymbol{\omega} + \boldsymbol{\omega}\cdot\boldsymbol{\nabla}\boldsymbol{v}. \tag{2}$$

If we have the velocity field $\boldsymbol{v}$ in Ω at a certain instant of time, we can rewrite Eq. (2) as

$$\frac{\partial \boldsymbol{\omega}}{\partial t} = -\boldsymbol{v}\cdot\boldsymbol{\nabla}(\boldsymbol{\nabla}\times\boldsymbol{v}) + \nu\nabla^2(\boldsymbol{\nabla}\times\boldsymbol{v}) + (\boldsymbol{\nabla}\times\boldsymbol{v})\cdot\boldsymbol{\nabla}\boldsymbol{v} \tag{3}$$

and solve for $\boldsymbol{\omega}$ at each point of the discretization of Ω by integration of Eq. (3) using an ODE solver.

Now, let us revisit Eq. (1) but this time impose a given distribution for the vorticity field the rate of expansion:

$$\nabla^2 \boldsymbol{v} = \boldsymbol{\nabla}\mathscr{D} - \boldsymbol{\nabla}\times\boldsymbol{\omega}, \tag{4}$$

$$\boldsymbol{\nabla}\cdot\boldsymbol{v} = \mathscr{D}, \tag{5}$$

$$\boldsymbol{\nabla}\times\boldsymbol{v} = \boldsymbol{\omega}. \tag{6}$$

Here $\boldsymbol{\omega}$ is the vorticity field in Ω given by Eq. (3) and $\mathscr{D}$ is the corresponding rate of expansion (i.e. the divergence field). The KLE is essentially defined as a solution of Eq. (4) in its weak form under the simultaneous constraints (5) and (6).

Let us consider the orthogonal decomposition of the velocity field in its irrotational nonsolenoidal component $\boldsymbol{v}_{\mathscr{D}}$, its solenoidal nonirrotational component $\boldsymbol{v}_{\omega}$ and its irrotational and solenoidal (i.e., harmonic) component $\boldsymbol{v}_h$. Under prescribed boundary conditions for the normal component of the velocity and given distributions for the vorticity $\boldsymbol{\omega}$ and the rate of expansion $\mathscr{D}$, this decomposition $\boldsymbol{v} = \boldsymbol{v}_{\mathscr{D}} + \boldsymbol{v}_{\omega} + \boldsymbol{v}_h$ is uniquely determined (Batchelor, 2000, Section 2.7). Constraints (5) and (6) ensure that $\boldsymbol{v}_{\mathscr{D}}$ and $\boldsymbol{v}_{\omega}$ are properly solved:

$$\boldsymbol{\nabla}\cdot\boldsymbol{v} = \boldsymbol{\nabla}\cdot\boldsymbol{v}_{\mathscr{D}} = \mathscr{D}, \tag{7}$$

$$\boldsymbol{\nabla}\times\boldsymbol{v} = \boldsymbol{\nabla}\times\boldsymbol{v}_{\omega} = \boldsymbol{\omega}. \tag{8}$$

Now, applying the orthogonal decomposition to the total velocity field $\boldsymbol{v}$ in Eq. (4) we have

$$\begin{aligned}\nabla^2(\boldsymbol{v}_h+\boldsymbol{v}_{\mathscr{D}}+\boldsymbol{v}_\omega) &= \nabla^2\boldsymbol{v}_h+\boldsymbol{\nabla}(\boldsymbol{\nabla}\cdot\boldsymbol{v}_{\mathscr{D}})-\boldsymbol{\nabla}\times(\boldsymbol{\nabla}\times\boldsymbol{v}_\omega)\\ &= \boldsymbol{\nabla}\mathscr{D}-\boldsymbol{\nabla}\times\boldsymbol{\omega};\end{aligned} \tag{9}$$

substituting Eqs. (7) and (8) in Eq. (9) yields

$$\nabla^2\boldsymbol{v}_h=0, \tag{10}$$

which provides the solution of the harmonic component $\boldsymbol{v}_h$. Thus, the KLE construction ensures that all three components of the velocity field are properly solved.

For incompressible cases, such as discussed here, $\mathscr{D}$ is simply set to zero. For compressible cases, $\mathscr{D}$ can be a general distribution given by a solution analogous to Eq. (3) but for the divergence transport equation (i.e., the momentum equation in divergence form) together with a solution of the mass transport equation and adding to Eqs. (2) and (3) the terms eliminated by the application of the incompressibility condition.

Now, provided that we can find a way of imposing on the velocity field the no-normal-flow condition

$$\boldsymbol{v}\cdot\boldsymbol{n}=0, \tag{11}$$

and the no-slip condition

$$\boldsymbol{v}\cdot\boldsymbol{\tau}=0, \tag{12}$$

on the solid boundary $\partial\Omega$ in a way compatible with the vorticity distribution at that time, we obtain a compatible solution for the velocity. Then, from this velocity field we produce the right-hand side of Eq. (3) required to advance the time-integration process to the next step. In order to impose the no-normal-flow and no-slip conditions on $\partial\Omega$ together with the correspondingly compatible boundary conditions on the vorticity, we designed a scheme based on two consecutive solutions of the KLE, which goes as follows:

(i) given a velocity field for the previous time-step $\boldsymbol{v}^{n-1}$ (which is compatible with the correspondent vorticity field $\boldsymbol{\omega}^{n-1}$), compute the next vorticity field $\tilde{\boldsymbol{\omega}}^n$ by time integration of Eq. (3) at each node of the spatial discretization. $\tilde{\boldsymbol{\omega}}^n$ is still incompatible with the velocity boundary conditions on the solid surface $\partial\Omega$;
(ii) get $\tilde{\boldsymbol{\omega}}_0^n$ by setting homogeneous conditions on $\partial\Omega$ for $\tilde{\boldsymbol{\omega}}^n$ (e.g., setting to zero the nodal values of $\tilde{\boldsymbol{\omega}}^n$ on $\partial\Omega$ once a discretization has been obtained);
(iii) compute a *free-slip* velocity field, $\vec{\boldsymbol{v}}^n$,by solving the KLE (i.e., solving (4) in its week form under the simultaneous constraints (5)–(6), with $\mathscr{D}=0$); this solution uses $\tilde{\boldsymbol{\omega}}_0^n$ as input, applying only the no-normal-flow ($\boldsymbol{v}\cdot\boldsymbol{n}=0$) condition on $\partial\Omega$ with the normal derivative of the tangential velocity set to zero;
(iv) from $\vec{\boldsymbol{v}}^n$, compute the new vorticity field as $\boldsymbol{\omega}^n=\boldsymbol{\nabla}\times\vec{\boldsymbol{v}}^n$ applying both the no-normal-flow ($\boldsymbol{v}\cdot\boldsymbol{n}=0$) and the no-slip condition ($\boldsymbol{v}\cdot\boldsymbol{\tau}=0$) on $\partial\Omega$; thus, $\boldsymbol{\omega}^n$ is a modified vorticity field produced in response to the induced slip which is compatible with the velocity boundary conditions on $\partial\Omega$;
(v) compute the final velocity field $\boldsymbol{v}^n$, by solving again the KLE but this time using $\boldsymbol{\omega}^n$ as input and applying both the no-normal-flow and the no-slip condition on $\partial\Omega$; in this way, $\boldsymbol{v}^n$ gives the weak solution for the velocity field at time-step n, which satisfies the time-dependent boundary conditions for the velocity, and simultaneously, its correspondent vorticity field $\boldsymbol{\omega}^n$ is compatible with those velocity boundary conditions.

In steps (iii)–(v) we apply the corresponding time-dependent, Dirichlet conditions for the velocity on $\partial\Omega_\infty$, the *external* boundary of Ω in the far field.

It is interesting to note that all the physics of the problem is contained in step (i) and it is solved as an ODE problem on the vorticity. Steps (ii)–(v) are concerned with the computation of a spatial solution for the velocity field which is compatible with both: the time-evolved vorticity distribution obtained in (i) and the time-dependent boundary conditions for the velocity. Setting homogeneous conditions on $\partial\Omega$ in step (ii) makes the vorticity field consistent with the *free-slip* solution of the velocity field to be computed in step (iii). Then, enforcing of the no-slip condition on $\partial\Omega$ in step (iv) gives the vorticity values in the boundary in response to the induced slip. This is the analog of the *vorticity-creation process* typically found in the early hybrid and nonprimitive methods mentioned above. Thus, we obtain our compatible vorticity boundary conditions on the solid surface by sequence of two solutions of the KLE under a different set of velocity boundary conditions. These two projectional operations of integral character applied on the velocity field (and performed inside each time step) ensure that the vorticity evolves in time in a way compatible with the time-dependent velocity boundary values. The algorithmic sequence defined in (i)–(v) is repeatedly performed inside the time-iteration process commanded by an adaptive variable-stepsize ODE solver. As we shall see later, we tested a

predictor–corrector (ABM–PECE) solver and a fifth-order adaptive Runge–Kutta solver (Press et al., 2002). In both cases, solution is checked by the adaptive stepsize control by monitoring of local truncation error, which proved to be quite stable for this application.

The algorithmic sequence defined in (i)–(v) has the advantage of producing a complete decoupling between the time integration of the vorticity transport equation and the space solution of the Poisson equation for the velocity field. The linear spatial solution defined in Eqs. (4)–(6) (i.e., the KLE) can be implemented in just one variational formulation. This implementation leads to a global matrix which is independent both of time and of the particular constitutive relation of the continuum media. Then, this matrix can be factorized at the moment of assembling and its triangular factors used as many times as needed so long as we are using the same grid. As we said, this is so even for problems with different constitutive relations because all the physics of the problem is taken into account only in the time-integration process for the vorticity, i.e., the spatial solution is purely *kinematic*. Thus, the space solution performed at each time step reduces to a pair of back-substitution processes where we simply change the right-hand side vector of the linear system in order to impose consecutively the boundary conditions (11)–(12). This scheme simplifies the issue of obtaining the vorticity in order to satisfy the boundary conditions on the velocity. Note that it is not a purely local manipulation performed on the boundary, this double solution of the velocity field is calculated over the entire domain involving two projectional operations of nonlocal character.

2.4. Numerical implementation of the KLE method

For the discretization of the KLE in two-dimensional applications we used nine-node biquadratic isoparametric finite elements, which though "expensive" in computational terms possess a high convergence rate and, due to their biquadratic interpolation of the geometric coordinates, provide the additional ability of reducing the so-called skin-error on curvilinear boundaries when compared to linear elements [for a detailed description of the isoparametric-element technique and its corresponding interpolation functions see Bathe (1996)]. In order to combine the power of convergence of the nine-node quadrilateral isoparametric element with the geometrical ability of a triangular grid to create suitable non structured meshes with gradual and smooth changes of density, we implemented what we called tri-quadrilateral isoparametric elements (Ponta and Jacovkis, 2001, 2003). The tri-quadrilateral elements consist of an assembling of three quadrilateral nine-node isoparametric elements in which each triangle of a standard unstructured mesh is divided into. Fig. 1 shows a schematic example of a mesh of tri-quadrilateral finite elements obtained from the original triangular discretization.

Another advantage of the tri-quadrilateral scheme is that, by a previous condensation of the nodes that lie inside the triangle, we can significantly reduce the number of nodes to solve in the final system, subsequently recovering the values for the internal nodes from the solution on the non condensable nodes. Fig. 2 shows a schematic view of the internal topology of the tri-quadrilateral element including the in-triangle global numeration of the nodes and indicating the three nine-node subelements (I)–(III).

The internal nodes 13–19 may be expressed in terms of nodes 1–12 which lay on the elemental boundary following the classical procedure for elemental condensation (Bathe, 1996). This process of condensation allows us to reduce the size of the new system to solve to approximately a 40% of the original system. As it was mentioned above, none of the matrices involved in the finite element solution depend on ω nor t, so they can be computed once for a given mesh,

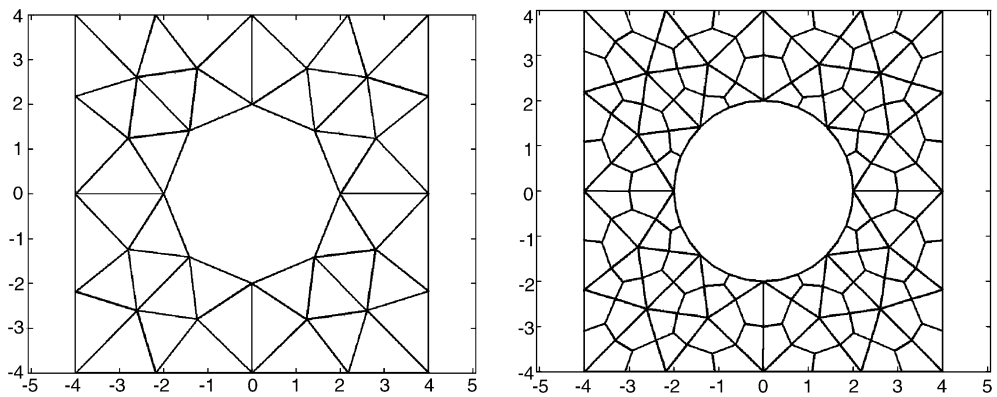

Fig. 1. An example of a mesh of tri-quadrilateral finite elements obtained from a standard triangular discretization.

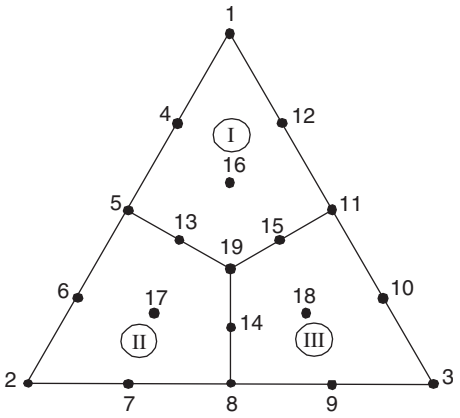

Fig. 2. Schematic view of the internal topology of the tri-quadrilateral element. Subelements (I)–(III) are model by standard nine-node isoparametric interpolation. Numbers 1–19 indicate the in-triangle nodal numeration.

stored and used as many times as needed to compute the solution for the discrete velocity field $\hat{V}$. The global matrix of the system is symmetric and positive definite, so it lends to factorization by Cholesky decomposition and its triangular factor is repeatedly used to solve $\hat{V}$ through back-substitution.

For the implementation of the time-integration procedure we evaluate the right-hand side of Eq. (3) applying the corresponding differential operators onto the discrete velocity field $\hat{V}$ calculated following steps (ii)–(v) in Section 2.3. The normal procedure to calculate derivatives on the nodes of a mesh of isoparametric elements consists in computing the derivatives in the Gaussian points adjacent to each node and interpolate their results following several alternatives techniques. A detailed description of this procedure can be found in Bathe (1996). In our case we used area-weighing interpolation which prove to be very effective. The contribution of each Gaussian point to its corresponding node depends on the constitution of the mesh and can be calculated at the moment of assembling. A set of arrays that perform the differential operations is assembled simultaneously with the finite-element matrices, so they can also be computed once for a given mesh, stored and used as many times as needed to provide evaluation of Eq. (3) right-hand side for an advanced package ODE solver. We choose a multivalue variable-order Adams–Bashforth–Moulton predictor–corrector (ABM–PECE) solver with adaptive stepsize control which proved to be quite efficient for this application. We also tried a fifth order adaptive-stepsize Runge–Kutta algorithm with good results. For the first DNS low-Reynolds-number applications of the KLE method, the function prove to be smooth enough for the adaptive ABM–PECE algorithm to work very efficiently, in these smooth cases the predictor–corrector outperforms other alternatives like the Bulirsch–Stoer method [see Press et al. (2002)].

The reader is asked to refer to Ponta (2005) where issues regarding the influence of the resolution of the spatial and time discretizations are addressed by a set of validation tests contrasting against analytical solutions and experimental results. In Ponta (2005), convergence tests were repeatedly performed for a succession of uniformly distributed unstructured meshes, progressively refined, and the max-norm and mean-norm of the error was evaluated. Ponta (2005) also includes comparison plots of the results produced by the KLE method and experimental measurements for the well-studied case of a circular cylinder started impulsively and then subjected to steady translational motion, finding an excellent agreement.

3. Numerical experiments on vortex wakes of an oscillating cylinder

Having explained the methodology, and established that it reproduces the known vortex wake phenomenology for a uniformly translating cylinder, we felt confident that we had a computational tool suitable for exploring aspects of wake formation from a cylinder executing an oscillatory motion in an otherwise stationary fluid. Fig. 3 shows an example of a mesh of tri-quadrilateral elements used.

In this section we report on our results regarding the formation, shedding and further evolution of vortex patterns produced in the wake of a cylinder executing forced oscillations for the range of Reynolds number below 180. This is, approximately, the periodic laminar wake regime for the usual, Kármán vortex street case. We concentrated on the case

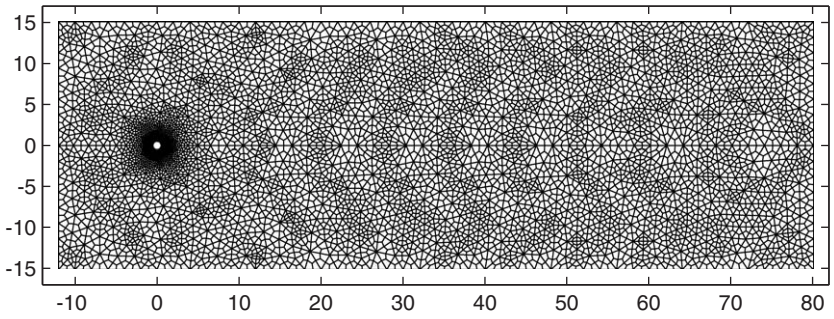

Fig. 3. An example of a mesh of tri-quadrilateral finite elements used for the present analysis (geometrical coordinates are given in diameters).

of $\mathrm{Re} = Ud/\nu = 140$ since this case is representative of the range and shows a variety of arrangements of vortex structures. In our exploration we were heavily influenced by the experimental study WR, mentioned in the Introduction, in which a classification of vortex wake patterns is proposed. WR construct a 'map' of vortex synchronization regions using as coordinates the nondimensional wavelength and nondimensional amplitude of the oscillations of the cylinder, i.e., the coordinates in the map are, λ/d, and A/d, where λ is the wavelength of the cylinder oscillations and A its amplitude. They observed that the $(\lambda/d, A/d)$ map is partitioned into 'synchronization regions', and they studied the case $\mathrm{Re} = 392$ in particular detail. In each 'synchronization region' a certain vortex wake pattern prevails, and WR denote these by symbols such as 'P + S', '2S', and '2P'. Here 'S' signifies a 'singlet' or single vortex, and 'P' signifies a pair of vortices of opposite signs. A pattern such as 'P + S', then, is one in which in each oscillation cycle the cylinder appears to shed a pair of vortices of opposite sign and a single vortex. Similarly, '2P' signifies a pattern in which two pairs are shed per cycle, '2S' a pattern in which two singlets are shed per cycle, and so on. The usual Kármán vortex street would simply be designated '2S' in this classification.

For two opposite vortices shed per cycle, the possible vortex wake patterns are quite limited and are all, essentially, versions of a vortex street (with variations in the ratio of downstream, i.e., inter-row, to intra-row spacing). The vortex wake patterns of an oscillating cylinder can be more complex than the Kármán street. As we noted in the opening section, we have started using the term 'exotic wakes' for these patterns. One may think of the system as a forced, nonlinear oscillator. The shedding frequency corresponding to the free stream velocity may be thought of as the 'natural' frequency of the system. The frequency of oscillation of the cylinder is an external forcing frequency. Due to the nonlinear coupling between these two oscillations a variety of combination frequencies can potentially be excited. Several of these frequencies may correspond to new wake patterns. Even if we restrict ourselves to cases where the wake pattern is stationary, i.e., the vortex configuration produced in each oscillation and shedding cycle is identical to that produced in the preceding oscillation/shedding cycle, there are many more possibilities already with three vortices per cycle than there are with two. A full classification of such patterns, assuming the vortices are point vortices, has recently been given by Stremler (2003).

According to the experiments reported by WR the $(\lambda/d, A/d)$ map at $\mathrm{Re} = 392$ is dominated by the vortex synchronization regions 'P + S' and 2P. WR note that the boundary between these regions depends on Reynolds number. Thus, at $\mathrm{Re} > 300$ part of the 'P + S' region is taken over by a '2P' region. At $\mathrm{Re} < 300$, where our numerical experiments are exclusively performed, the '2P' region contracts or disappears altogether. The boundaries between the various regions are difficult to determine experimentally and their theoretical basis is unclear. However, we have a crude argument that (a) produces delineations in the WR map that are not altogether dissimilar from the boundary curves between vortex synchronization regions, and (b) may help to explain how and why the regions shift with Reynolds number. We also found another structure which we can call a hyper-Kármán vortex street produced by the coalescence of pairs of smaller vortices into a new Kármán-like arrangement. This structure is produced when the cylinder oscillates following a constant-speed trajectory (here $\mathrm{Re} = Ud/\nu = 140$ is defined based on the constant tangential speed of the cylinder). We pause to develop these ideas in the next two subsections.

3.1. On the boundaries between vortex synchronization regions in the WR map

WR observed that the $(\lambda/d, A/d)$ map correctly represents the synchronization regions for the range $300 < \mathrm{Re} < 1000$. Now, the Strouhal number for the case of a nonoscillating cylinder remains nearly constant in the $300 < \mathrm{Re} < 1000$

range. For $\mathrm{Re} > 300$ the St–Re curve asymptotes to a constant value of $\mathrm{St} = 0.2$, approximately. Thus, in the oscillator analogy, the 'natural frequency' of the system is largely fixed, and only the 'forcing frequency' varies. Assuming a constant value of $\mathrm{St} = 0.20$ throughout the range, it is possible to establish a correspondence between the nondimensional wavelength λ/d and the ratio between the period of the forced oscillation ($T_e = \lambda/U$) and the period of vortex shedding for a nonoscillating cylinder ($T_s = d/(U\,\mathrm{St})$), viz. $T_e/T_s = \mathrm{St}\,\lambda/d = 0.20\lambda/d$. This correspondence allows one to think of λ/d as a measure of the period of the forced oscillation scaled by what we may call the period of natural oscillation of the system (i.e., the period of the Kármán vortex street for a nonoscillating cylinder).

On the other hand, for $\mathrm{Re} < 300$, and certainly for $\mathrm{Re} = 140$ where most of our numerical simulations were conducted, the Kármán shedding frequency varies quite considerably with Reynolds number. Now, in an oscillatory motion of the cylinder, with a fixed towing speed in the upstream direction, the speed of the cylinder relative to the fluid through which it is being moved varies, and the effective Re of the cylinder motion along its trajectory fluctuates. For $\mathrm{Re} < 300$, the strong dependence of St implies that the period of natural oscillation changes considerably. Moreover, the amplitude of that fluctuation depends on the nondimensional parameters λ/d and A/d, so it will vary throughout the map; see Ponta and Aref (2005). To see the potential consequences of this variation, consider the following motion of the cylinder center:

$$x_{cy}(t) = Ut, \tag{13}$$

$$y_{cy}(t) = A\,\sin\left(2\pi\,\frac{t}{T_e}\right) = A\sin\left(2\pi\,\frac{tU}{\lambda}\right). \tag{14}$$

The corresponding velocities are

$$V_{xcy}(t) = U, \tag{15}$$

$$V_{ycy}(t) = 2\pi U\,\frac{A}{\lambda}\cos\left(2\pi\,\frac{tU}{\lambda}\right). \tag{16}$$

The peak value for the speed of the cylinder along its trajectory is

$$\hat{U} = U\sqrt{1 + \left(2\pi\,\frac{A}{\lambda}\right)^2}, \tag{17}$$

with a corresponding peak value for the associated Reynolds number,

$$\hat{\mathrm{Re}} = \frac{\mathrm{d}}{\nu}\,U\sqrt{1 + \left(2\pi\,\frac{A}{\lambda}\right)^2} = \mathrm{Re}\sqrt{1 + \left(2\pi\,\frac{A}{\lambda}\right)^2}. \tag{18}$$

The deviation of the instantaneous vortex shedding period, T_s, from its value corresponding to peak Reynolds number, relative to the period of forced oscillation, $T_e = \lambda/U$, is

$$\Delta = \frac{T_s - \hat{T}_s}{T_e} = \frac{(d/U\,\mathrm{St}) - (d/U\,\hat{\mathrm{St}})}{\lambda/U} = \frac{1/\mathrm{St} - 1/\hat{\mathrm{St}}}{\lambda/d}, \tag{19}$$

where $\hat{T}_s$ and $\hat{\mathrm{St}}$ are the shedding period and Strouhal number associated with $\hat{\mathrm{Re}}$. Taking the St–Re relation summarized in the experimental best-fit line given in Roshko (1954),

$$\mathrm{St} = \begin{cases} 0.212(1 - 21.1/\mathrm{Re}), & \mathrm{Re} < 180, \\ 0.212(1 - 12.7/\mathrm{Re}), & \mathrm{Re} > 300. \end{cases} \tag{20}$$

Substituting it into Eq. (19) and then using Eq. (18), we finally have,

$$\Delta = \begin{cases} \dfrac{1}{0.212\lambda/d}\left(\left(1-\dfrac{21.1}{\mathrm{Re}}\right)^{-1} - \left(1-\dfrac{21.1}{\mathrm{Re}\sqrt{1+\left(2\pi\dfrac{A/d}{\lambda/d}\right)^2}}\right)^{-1}\right), & \mathrm{Re}<180, \\ \dfrac{1}{0.212\lambda/d}\left(\left(1-\dfrac{12.7}{\mathrm{Re}}\right)^{-1} - \left(1-\dfrac{12.7}{\mathrm{Re}\sqrt{1+\left(2\pi\dfrac{A/d}{\lambda/d}\right)^2}}\right)^{-1}\right), & \mathrm{Re}>300, \end{cases} \tag{21}$$

which gives Δ in terms of Re and the parameters of the $(\lambda/d, A/d)$ map.

Fig. 4(a) shows the original map as presented in WR on which we have superimposed the 0.001, 0.015 and 0.06 isolines of Δ for $\mathrm{Re} = 392$, a value of Re that is representative of the range of Reynolds numbers for which the WR map is valid. We chose these particular values for the isolines because they roughly coincide with the 2P and P + S region boundaries. This coincidence suggests that the vortex synchronization region boundaries are, somehow, associated with definite fluctuation levels in the 'natural frequency' of shedding for the cylinder. These fluctuations arise due to the oscillatory changes in the speed of the cylinder relative to the background fluid.

Fig. 4(b) shows the same map but with isolines of Δ for $\mathrm{Re} = 140$ superimposed. We notice that the zone of Δ between the 0.015 and 0.06 isolines, which in the original WR map corresponded to P + S states, has now rotated clockwise down to the right, and occupies the region where the 2P states were before. Furthermore, the region between the 0.001 and 0.015 isolines, corresponding previously to 2P states, has moved further down to the point where it almost has fallen out of the region where the 2P patterns were previously observed. Thus, if we again assume that the boundaries of the different vortex synchronization regions are, somehow, associated with isolines of Δ, this would explain why the 2P state is not observed at low Reynolds numbers and the P + S state takes its place, i.e., the level of fluctuation of the shedding frequency is apparently too high to produce a 2P pattern, which for reasons that we do not fully comprehend is more sensitive to 'detuning' than P + S. Note that for these lower Reynolds numbers the Strouhal number is much more sensitive to changes in Reynolds number than is the case at higher Reynolds number. This speculative line of reasoning is consistent with the idea that the 2P and P + S states depend on similar mechanisms for their generation, but these mechanisms requires a finer balance for a 2P wake to be produced than for a P + S wake. The experimental observations by WR indicate that a 2P wake depends on a splitting of the region of vorticity that is being shed due to the straining by neighboring vortices. Thus, instead of having one vortex pair in each cycle, we produce two pairs. As we show below, in the P + S wake, even when regions of both signs of vorticity in the near wake are stretched, only one of them splits while the other remains strong enough to 'recover', and we produce just three vortices per cycle. In both cases a vortex splitting process is key to forming the vortex wake structure, but it is reasonable to assume that the mutual influence of regions of positive and negative vorticity necessary for the 2P pattern might require a higher degree of synchrony and thus be the more sensitive to fluctuation levels in time scales or frequencies.

3.2. *Formation of* P + S *vortex streets at low Reynolds number*

In Fig. 4(b), we have indicated the parameter sets explored in our study. Point *A1* ($\lambda/d = 7.5, A/d = 1$) produced the clearest P + S arrangement. In Fig. 5, we show a comparison of a gray scale plot of the vorticity field produced by the kinematic Laplacian equation method for point *A1* with an unpublished experimental laser-fluorescene photograph for an oscillating cylinder with $\mathrm{Re} = 140$, $\lambda/d = 6.07$, and $A/d = 0.5$. This photo was kindly provided by Prof. C. H. K. Williamson.

Fig. 6 shows the nondimensional vorticity field for point *A1*. We checked that for each triplet the sum of the circulation of the two positive vortices equals the opposite of the circulation of the negative vortex, so the complete circulation produced in one cycle is very close to zero. Fig. 7 shows a sequence plot of the nondimensional vorticity field during the vortex splitting process that produces the P + S pattern. Starting at the bottom-left panel, and following the sequence clockwise, we see how the positive (lower) half of the near wake is stretched by the strain rate field of the neighboring vortices until it breaks into two separated vortices. If we follow the evolution of the negative (upper) half of the near wake, we notice that it also starts to split in two but, contrary to what happens to its positive counterpart, a

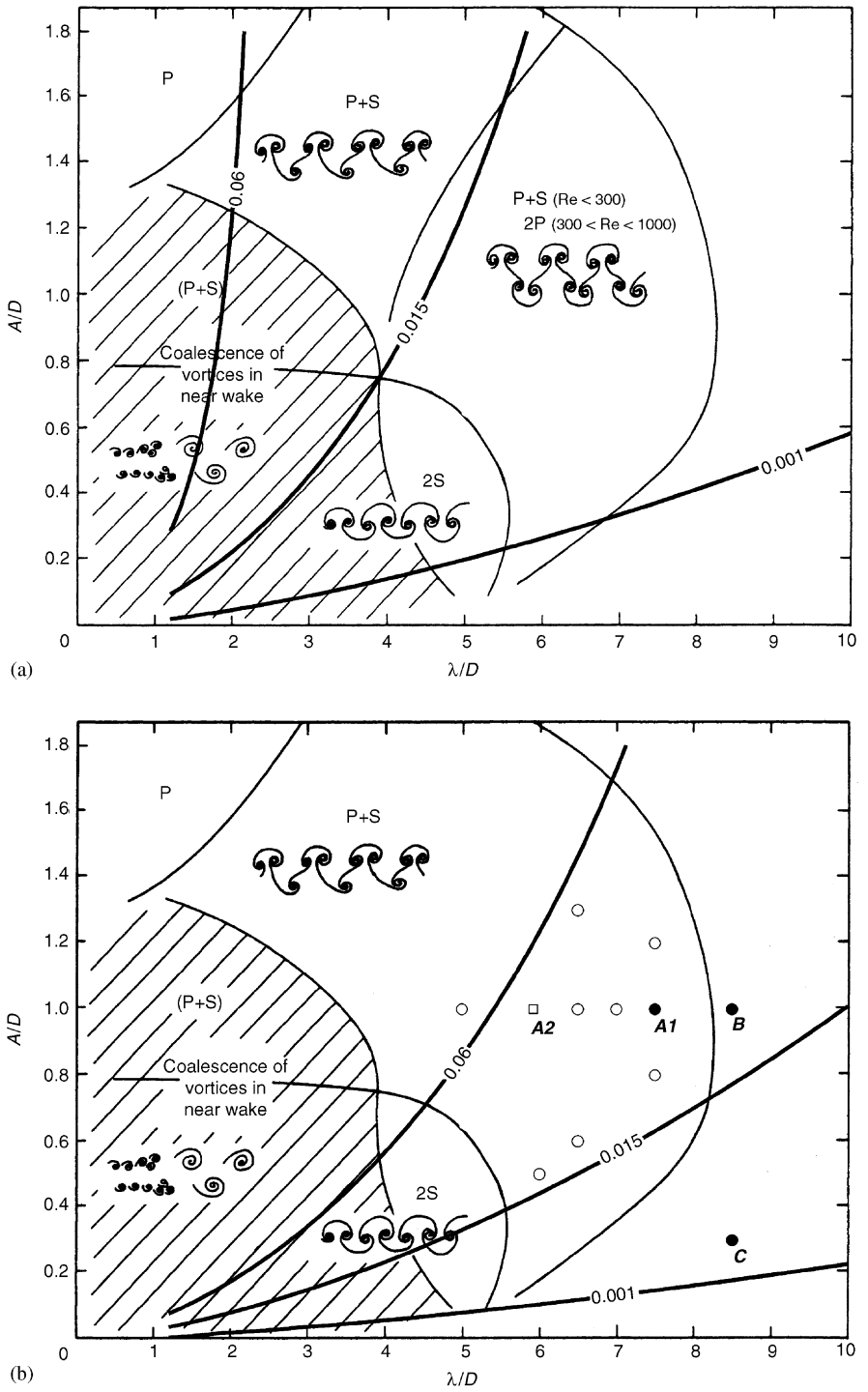

Fig. 4. Original $(\lambda/d, A/d)$ map from Williamson and Roshko (1988) including the 0.001, 0.015 and 0.06 isolines of Δ (defined in the text) for (a) $\mathrm{Re} = 392$ and (b) $\mathrm{Re} = 140$. Panel (b) also includes the location of the parameter choices used in the numerical experiments. The labelled markers indicate points of particular interest which are referred to in the text.

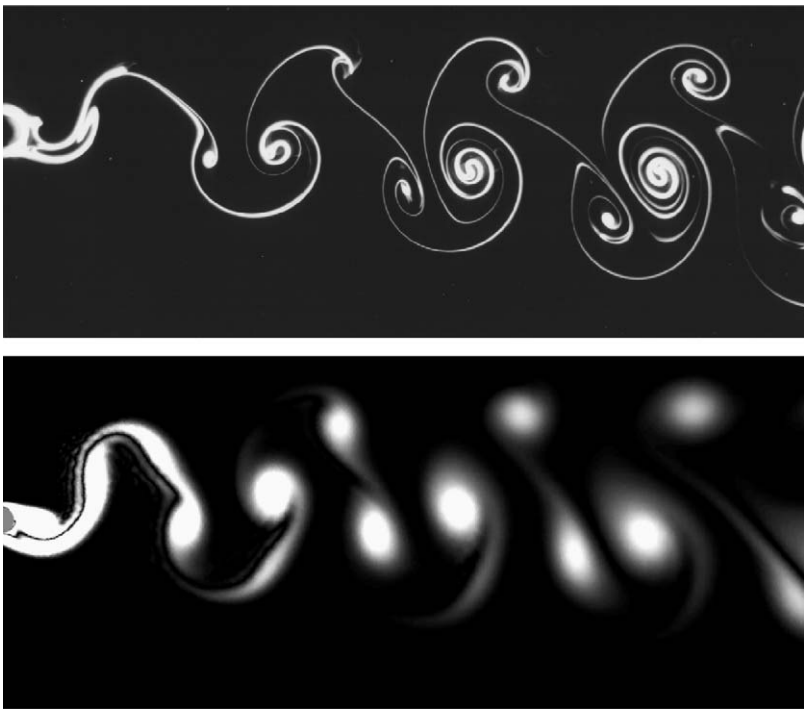

Fig. 5. Comparison of flow visualization of a P + S wake of an oscillating cylinder for Re = 140 by C. H. K. Williamson (private communication) with a gray scale plot of the vorticity field produced by the kinematic Laplacian equation method at the same Reynolds number.

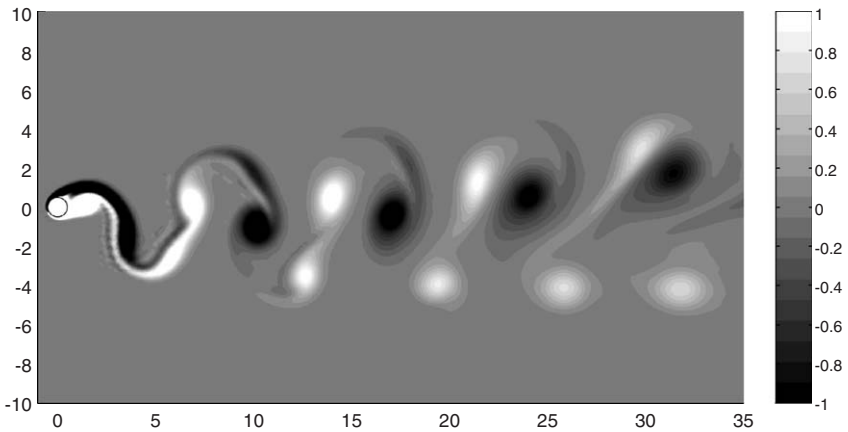

Fig. 6. Nondimensional vorticity field of the P + S wake for Re = 140, $\lambda/d = 7.5$, and $A/d = 1$, calculated by the kinematic Laplacian equation method. This figure corresponds to Fig. 5 flipped about a horizontal axis.

major portion of the shed vorticity remains together, and this vorticity forms a vortex that is strong enough to recover its 'tail'. This last process takes longer than the splitting and completes the sequence of close-up views used in Fig. 7. We can follow the successive triplet structures as they progress and evolve downstream in Fig. 6.

The empty circles in Fig. 4(b) correspond to various parameter sets explored, some of which showed a P + S structure with a weaker pattern than point *A1*. For example, Fig. 8 shows the nondimensional vorticity field for point *B* ($\lambda/d = 8.5$, $A/d = 1$), which may be taken as a representative of a weak P + S mode. Notice that the weak, upper,

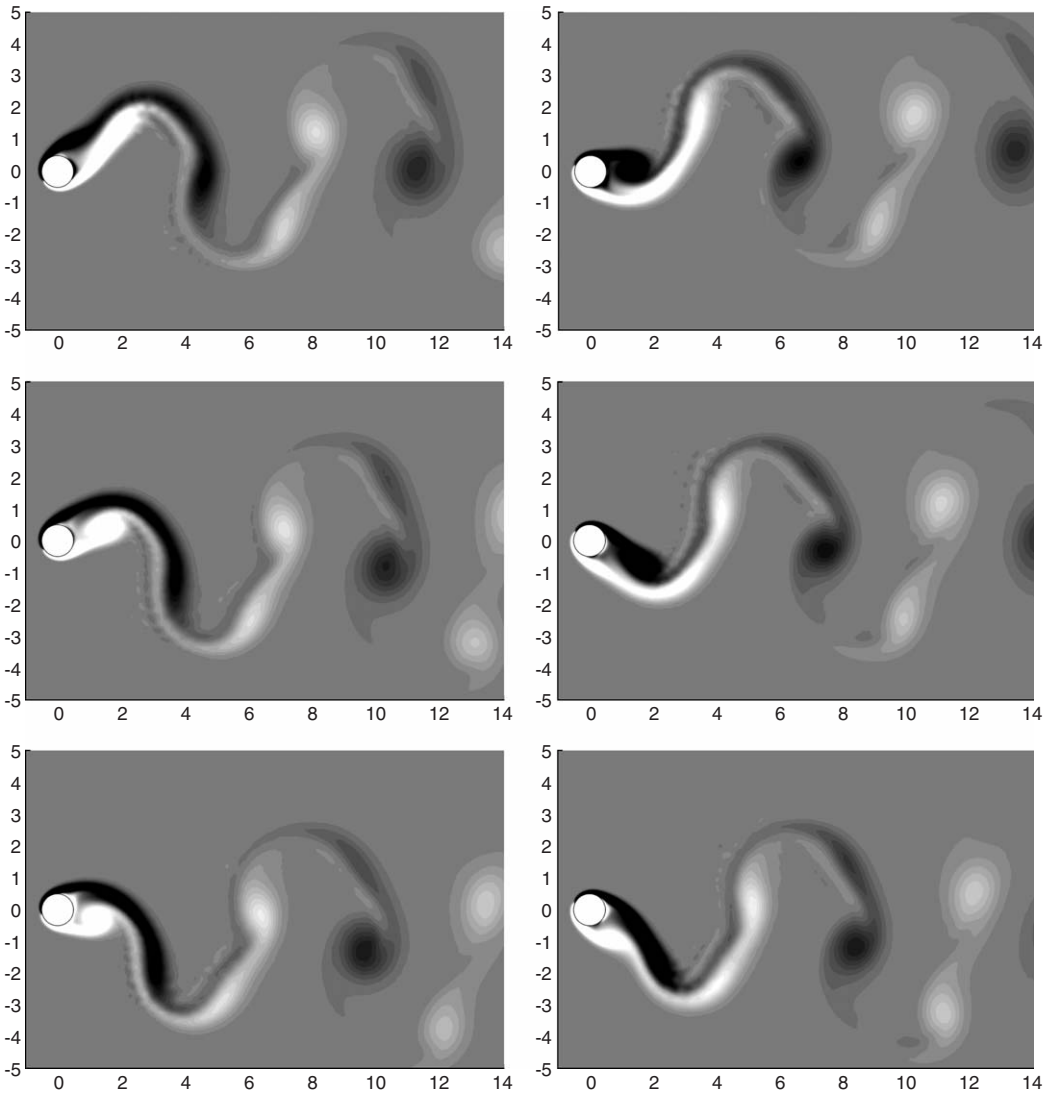

Fig. 7. Sequence plot of the vortex splitting process that produces the P + S pattern. The sequence begins at the bottom left panel and may be followed by viewing the other panels clockwise.

positive vortex in the structure is not recovered by the strong, lower, positive vortex and remains independent (so the pattern is still a P + S) but the third vortex tends to dissipate quickly as the wake moves downstream.

Point C ($\lambda/d = 8.5, A/d = 0.3$) lies far out of the P + S region, in a zone marked as 'no synchronized pattern observed' in the WR map. Fig. 9 shows the nondimensional vorticity field for this case with its unorganized pattern of vortices. This is consistent with the experimental observations.

3.3. Constant-speed trajectory and a 'hyper-Kármán vortex-street'

In an attempt to reduce the effects of the fluctuations of the speed of the cylinder along its trajectory, we moved the cylinder along a new path in which the speed of motion relative to the fluid is kept constant. The expression for the tangential speed of the cylinder U_{tg} is

$$U_{tg} = \sqrt{V_{x,cy}^2 + V_{y,cy}^2}. \tag{22}$$

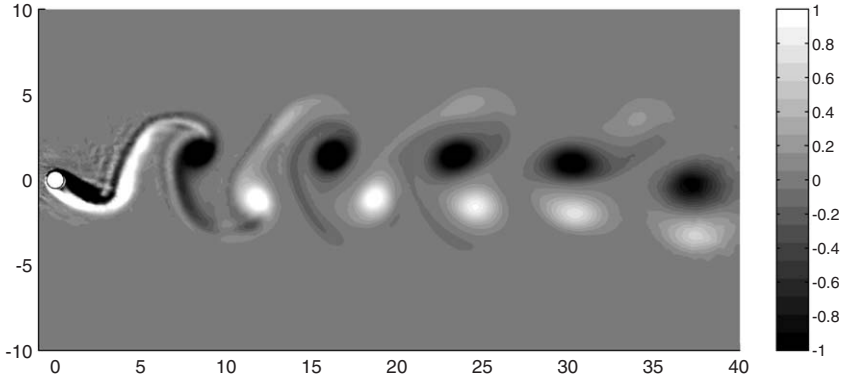

Fig. 8. Nondimensional vorticity field of the weak P + S wake for Re = 140 ($\lambda/d = 8.5$, $A/d = 1$).

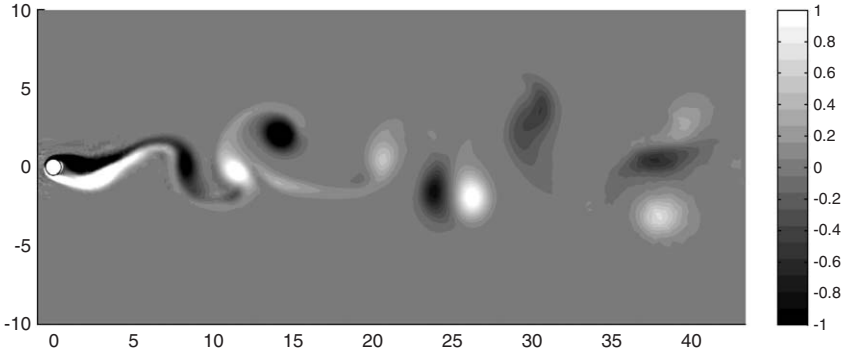

Fig. 9. Nondimensional vorticity field of an unorganized wake pattern for Re = 140 ($\lambda/d = 8.5, A/d = 0.3$).

Keeping the same vertical speed (in order to keep the same period of forced oscillation) and adjusting the horizontal component of the velocity to keep U_{tg} constant and equal to the reference speed U, we have

$$V_{x,cy} = U\sqrt{1 + \left(2\pi \frac{A}{\lambda}\cos\left(2\pi \frac{tU}{\lambda}\right)\right)^2}. \tag{23}$$

Fig. 10 shows an example of a constant-speed path for the set of parameters of point *A1* ($\lambda/d = 7.5, A/d = 1$). Panel (a) shows one cycle starting from the upper part of the path. The geometrical coordinates are given in diameters, the solid line indicates the path of the center of the cylinder and the dotted circles show its circumference. The average horizontal speed $U_{x,m}$ for this set of parameters equals 0.789 of the reference speed U. Fig. 10(b) shows the trajectory of the cylinder with respect of a reference frame moving horizontally at constant speed U_{xm}. Although this motion nominally has the same values of λ and A as before, the cylinder really has acquired a slight streamwise oscillation relative to the steady translation of the earlier motion.

Fig. 11 shows the nondimensional vorticity field for the constant-speed path for the set of parameters of point *A1*. In this case, we have two single vortices shed in each cycle and the wake initially shows a relatively well-defined and close-packed Kármán arrangement that extends downstream for a distance of about 10 diameters. Thus, for the range of parameters that for the variable speed trajectory produces the P + S wake, the constant-speed counterpart of that trajectory produces a symmetric wake in which the asymmetric splitting process has disappeared and a more regular (and perfectly symmetric) primary vortex street ensues. This proves our hypothesis that the speed-fluctuations play an important role in the splitting process and affect the symmetry of the primary wake, which is responsible of producing a P + S wake instead of a 2P.

Later, however, a process of merging of neighboring vortices within either row takes place. This process form a set of larger vortices with twice the downstream and cross-stream spacing of the original street and that we may call a

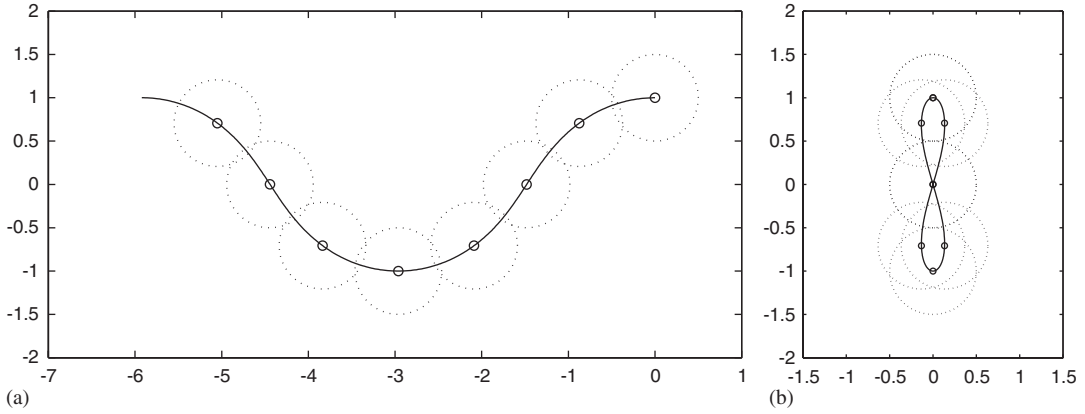

Fig. 10. (a) Constant-speed path for the set of parameters of point A1 ($\lambda/d = 7.5, A/d = 1$), (b) the same path in a frame moving with the average horizontal speed U_{xm}.

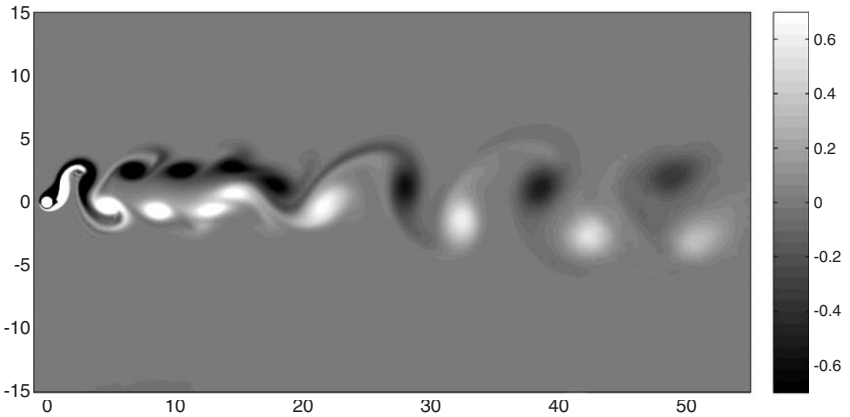

Fig. 11. Nondimensional vorticity field of the 'hyper-Kármán vortex-street' for Re = 140, $\lambda/d = 7.5$, and $A/d = 1$, calculated by the kinematic Laplacian equation method.

'hyper-Kármán vortex-street'. Fig. 12 shows a sequence of plots of the nondimensional vorticity field during the vortex-merging process. Starting at the bottom-left panel and following clockwise as before (in this case each loop around the panels of the figure corresponds to two cycles of the oscillation), we see how the near wake produces two separated vortex units per cycle that arrange as a close-packed Kármán street, then the later pair of this initial arrangement is absorbed by the next pair to form the bigger structures which halve the frequency of the forced oscillation.

The formation of a secondary vortex street in the wake of a stationary cylinder in a uniform stream was observed by Taneda (1959) by using flow visualization techniques. In these experiments the primary Kármán vortex street decays downstream, and the secondary vortex street is formed with a larger scale of vortices (and thus a lower frequency) than those in the primary Kármán street. Cimbala et al. (1988) and Williamson and Prasad (1993) also studied the mechanism of formation of the secondary vortex street in unforced wakes. Matsui and Okude (1983) experimented with flow visualization and hot-wire measurements on acoustically forced cylinder wakes, observing that a secondary vortex street is formed as a result of merging of the primary Kármán vortices. When the wake was forced acoustically by one half or one third of the frequency of the Kármán vortices, every two or every three vortices merged. Aref and Siggia (1981) and Meiburg (1987), studied numerically the formation of the secondary vortex street applying subharmonic perturbations to vortex blobs of opposite sign that model the Kármán street. In both cases, vortex merging was observed, which suggests its importance for the formation of the secondary street. Inoue and Yamazaki (1999) solved the Navier–Stokes equations using finite differences and observed the merging-by-pairing process in the wake of

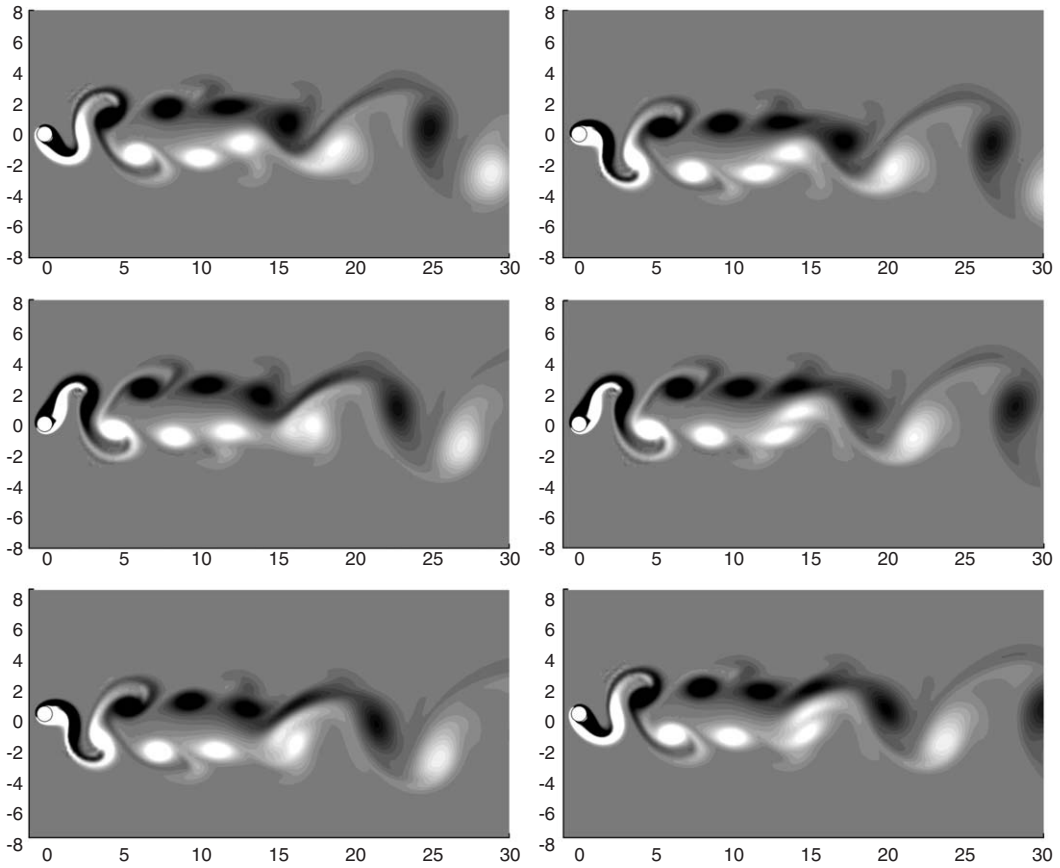

Fig. 12. Sequence plot of the vortex–merging process that produces the 'hyper-Kármán vortex-street'. The sequence begins at the bottom left panel and may be followed clockwise through the remaining panels.

stationary cylinders in a perfect uniform stream when an in-line sinusoidal perturbation was added. The forced wake cases mentioned above, could be somewhat analogous to a trajectory combining an in-line oscillation of the cylinder with a constant speed displacement (there was no vertical component of the motion). It is interesting to note that for many of the cases where a merging process is involved, some sort of in-line fluctuation is applied. In our case, even in the presence of a stronger vertical oscillation, the in-line component necessary to keep the tangential speed constant is apparently enough to induce merging. We suggest that the packing–unpacking process of the vortices in the primary street is due to the in-line fluctuation which destabilizes the Kármán array and triggers merging. The presence of a vertical oscillation is not trivial, because it causes the frequency of the primary wake to be the one set by the vertical forced oscillation, whereas in the previous studies the frequency of the primary wake corresponds to the shedding frequency leading to an ordinary Kármán street.

Finally, there is another issue that should be taken into account in the case of the constant-speed path. For the trajectory with constant streamwise speed, we use U as a reference speed to define both the Reynolds number and the geometrical wavelength λ, which also corresponds to the period of the forced oscillation ($\lambda = T_e U$). Thus, we may interpret the parameter λ/d both as a nondimensional geometrical wavelength and as a nondimensional period of forced oscillation ($\lambda/d = T_e U/d$). With the constant-speed path, on the other hand, we should use the tangential speed U_{tg} to define the Reynolds number and the nondimensional period of the forced oscillation, but now the geometrical wavelength must be defined in terms of the average horizontal speed ($\lambda_g = T_e U_{xm}$). This introduces a new aspect concerning the WR map, as the parameter λ/d has a dual interpretation. For example, if we interpret λ/d as a nondimensional period of the forced oscillation, the case analyzed above remains in its original location at point *A1*. However, if we interpret λ/d as a nondimensional geometrical wavelength, we move to point *A2* in the WR map, which we marked by an empty square in Fig. 4(b).

4. Concluding remarks

We have introduced a mathematical–computational approach to solving flows in a frame of reference attached to a moving body and we have used this tool to explore the vortex synchronization regions in the amplitude–wavelength map of WR for low Reynolds number, focusing on the process of splitting which characterizes the formation of the P + S and 2P structures. We proposed a parameter to quantify the level of fluctuation of the natural frequency of the system and this may shed some light on the 2P–P + S problem mentioned in the Introduction.

WR observed coalescence into a large-scale, Kármán-like arrangement of a large number of small vortices produced at high frequencies of the forced oscillation for sinusoidal trajectories. Working with constant-speed trajectories, we found the 'hyper-Kármán vortex street' arrangement. This phenomenon, characterized by a pairwise merging process at low frequency that produces a duplication of the period, is, to the best of our knowledge, reported here for the first time for a moving, vertically oscillating cylinder. The synchronization of our primary vortex street with the vertical forced oscillation instead of with the Kármán shedding suggests that the pairwise merging phenomenon itself is related to the structure of the primary street (through the spacing of the vortices) rather than to the original process that generated the primary street.

Based on point vortex models we are convinced that there exist a multitude of more complex vortex wake patterns (exotic wakes) than have so far been seen in experiments. Although we understand how to 'set these up' if we had complete control over how to distribute the vorticity in the flow, we do not yet understand how to produce such vortex wakes by oscillation and rotation of a wake-producing bluff body. We hope to use the numerical tool developed here for such explorations in the future. It is entirely possible that the purely two-dimensional problem (whatever its relevance) behaves a bit differently than the problem of a predominantly two-dimensional wake in a three-dimensional world. Nevertheless, we believe the current numerical exploration is useful for understanding the experiments that have been performed and a valuable guide for designing future experiments.

Regarding the KLE method itself, we wish to emphasize its economy of computational effort compared to more classical velocity–pressure approaches due to its vorticity-in-time/velocity-in-space split nature. More important is its flexibility to manage different trajectories with translational and rotational acceleration [the invariance of the vorticity–velocity formulation under acceleration of the frame of reference is fully addressed in Speziale (1987)]. Besides, its substantial tolerance to the use of unstructured meshes allows a more suitable *meshing* of complex geometries than structured-mesh approaches would permit. Thus, this method gives us a useful tool to study the vortex structure of wakes for different body shapes and motions. Since it is a new approach, we are still exploring its capabilities to manage higher-Reynolds-number flows in direct numerical simulation, and its potential to be extended to large eddy simulation applications. As we have mentioned above, the basic formulation is three-dimensional and has no special requirements on the divergence field, so the method can be extended to compressible flows and to three-dimensional analysis.

Acknowledgments

F. L. Ponta is very grateful to the University of Buenos Aires for granting him a leave in order to complete this work. He would like to acknowledge the hospitality of the Department of Theoretical and Applied Mechanics at University of Illinois. This work was funded in part by research funds made available by University of Illinois.

References

Anagnostopoulos, P., Bearman, P.W., 1992. Response characteristics of a vortex-excited cylinder at low Reynolds numbers. Journal of Fluids and Structures 6, 39–50.

Anderson, C.R., 1988. Observations on vorticity creation boundary conditions. In: Caflisch, R.E. (Ed.), Mathematical Aspects of Vortex Dynamics. SIAM, Philadelphia, PA, pp. 144–159.

Aref, H., Siggia, E., 1981. Evolution and breakdown of a vortex street in two dimensions. Journal of Fluid Mechanics 109, 435–463.

Aref, H., Stremler, M.A., 1996. On the motion of three point vortices in a periodic strip. Journal of Fluid Mechanics 314, 1–25.

Batchelor, G.K., 2000. An Introduction to Fluid Dynamics. Cambridge University Press, Cambridge.

Bathe, K.J., 1996. Finite Element Procedures. Prentice-Hall, Englewood Cliffs, NJ.

Blackburn, H., Henderson, R., 1996. Lock-in behavior in simulated vortex-induced vibration. Experimental Thermal and Fluid Science 12, 184–189.

Chorin, A.J., 1973. Numerical study of slightly viscous flow. Journal of Fluid Mechanics 57, 785–796.

Chorin, A.J., 1978. Vortex sheet approximation of boundary layers. Journal of Computational Physics 27, 428–442.
Cimbala, J.M., Nagib, H.M., Roshko, A., 1988. Large structure in the far wakes of two-dimensional bluff bodies. Journal of Fluid Mechanics 190, 265–298.
Clercx, H.J.H., 1997. A spectral solver for the Navier–Stokes equations in the velocity–vorticity formulation for flows with two nonperiodic directions. Journal of Computational Physics 137, 186–211.
Davies, C., Carpenter, P.W., 2001. A novel velocity–vorticity formulation of the Navier–Stokes equations with applications to boundary layer disturbance evolution. Journal of Computational Physics 172, 119–165.
Dennis, S.C.R., Ingham, D.B., Cook, R.N., 1979. Finite difference methods for calculating steady incompressible flows in three dimensions. Journal of Computational Physics 33, 325–339.
Evangelinos, C., Karniadakis, G.E., 1999. Dynamics and flow structures in the turbulent wake of rigid and flexible cylinders subject to vortex-induced vibrations. Journal of Fluid Mechanics 400, 91–124.
Fasel, H., 1976. Investigation of the stability of boundary layers by a finite difference model of the Navier–Stokes equations. Journal of Fluid Mechanics 78, 355–383.
Gatski, T.B., Grosh, C.E., Rose, M.E., 1989. The numerical solution of the Navier–Stokes equations for 3-dimensional unsteady incompressible flows by compact schemes. Journal of Computational Physics 82, 298–329.
Griffin, O.M., Ramberg, S.E., 1974. The vortex street wakes of vibrating cylinders. Journal of Fluid Mechanics 66, 553–576.
Guevremont, G., Habashi, W.G., Kotiuga, P.L., Hafez, M.M., 1993. Finite element solution of the 3D compressible Navier–Stokes equations by a velocity–vorticity method. Journal of Computational Physics 107, 176–187.
Guj, G., Stella, F., 1993. A vorticity–velocity method for the numerical solution of 3D incompressible flows. Journal of Computational Physics 106, 286–298.
Inoue, O., Yamazaki, T., 1999. Secondary vortex streets in two-dimensional cylinder wakes. Fluid Dynamics Research 25, 1–18.
Khalak, A., Williamson, C.H.K., 1999. Motion forces and mode transitions in vortex-induced vibration at low mass-damping. Journal of Fluids and Structures 13, 813–851.
Lo, D.C., Young, D.L., 2004. Arbitrary Lagrangian–Eulerian finite element analysis of free surface flow using a velocity–vorticity formulation. Journal of Computational Physics 195, 175–201.
Matsui, T., Okude, M., 1983. Formation of the secondary vortex street in the wake of a circular cylinder. In: IUTAM Symposium on Structures of Compressible Turbulent Shear Flows, Marseille. Springer, Berlin, pp. 156–164.
Meiburg, E., 1987. On the role of subharmonic perturbations in the far wake. Journal of Fluid Mechanics 177, 83–107.
Meneghini, J.R., Bearman, P.W., 1995. Numerical simulation of high amplitude oscillatory flow about a circular cylinder. Journal of Fluids and Structures 9, 435–455.
Mittal, S., Kumar, V., 1999. Numerical simulation of high amplitude oscillatory flow about a circular cylinder. International Journal of Numerical Methods in Fluids 31, 1087–1120.
Mittal, S., Tezduyar, T.E., 1992. A finite element study of incompressible flows past oscillating cylinders and airfoils. International Journal of Numerical Methods in Fluids 15, 1073–1118.
Napolitano, M., Pascazio, G., 1991. A numerical method for the vorticity–velocity Navier–Stokes equations in two and three dimensions. Computational Fluids 19, 489–495.
Newman, D.J., Karniadakis, G.E., 1996. Simulations of flow over a flexible cable: a comparison of forced and flow-induced vibration. Journal of Fluids and Structures 10, 439–453.
Newman, D.J., Karniadakis, G.E., 1997. A direct numerical simulation study of flow past a freely vibrating cable. Journal of Fluid Mechanics 344, 95–136.
Ponta, F.L., 2005. The kinematic Laplacian equation method. Journal of Computational Physics 207, 405–426.
Ponta, F.L., Aref, H., 2005. Vortex synchronization regions in shedding from an oscillating cylinder. Physics of Fluids 17, 011703.
Ponta, F.L., Jacovkis, P.M., 2001. A vortex model for Darrieus turbine using finite element techniques. Renewable Energy 24, 1–18.
Ponta, F.L., Jacovkis, P.M., 2003. Constant-curl Laplacian equation: a new approach for the analysis of flows around bodies. Computational Fluids 32, 975–994.
Press, W.H., Teukolsky, S.A., Vetterling, W.T., Flannery, B.P., 2002. Numerical Recipies in C, second ed. Cambridge University Press, Cambridge.
Quartapelle, L., 1981. Vorticity conditioning in the computation of two-dimensional viscous flows. Journal of Computational Physics 40, 453–477.
Quartapelle, L., 1993. Numerical Solution of the Incompressible Navier–Stokes Equations. Birkäuser, Basel, Switzerland.
Quartapelle, L., Valz-Gris, F., 1981. Projections conditions on the vorticity in viscous incompressible flows. International Journal of Numerical Methods in Fluids 1, 129–144.
Roshko, A., 1954. On the development of turbulent wakes from vortex streets. TR 1191, NACA.
Speziale, C.G., 1987. On the advantages of the velocity–vorticity formulation of the equations of fluid dynamics. Journal of Computational Physics 73, 476–480.
Stremler, M.A., 2003. Relative equilibria of vortex arrays, preprint.
Taneda, S., 1959. Downstream development of the wakes behind cylinders. Journal of Physics Society of Japan 14, 843–848.
Williamson, C.H.K., Prasad, A., 1993. A new mechanism for oblique wave resonance in the natural far wake. Journal of Fluid Mechanics 256, 269–313.
Williamson, C.H.K., Roshko, A., 1988. Vortex formation in the wake of an oscillating cylinder. Journal of Fluids and Structures 2, 355–381.